Ultra-wideband SAR Tomography on asteroids

Oriane Gassot[1], Alain Herique[1], Wenzhe Fa[2,3], Jun Du[2] and Wlodek Kofman[1, 4]

[1]Univ. Grenoble Alpes, CNRS, CNES, IPAG, 38000 Grenoble, France

[2]Institute of Remote Sensing and Geographical Information System, School of Earth and Space Sciences, Peking University, Beijing, China

[3]State Key Laboratory of Lunar and Planetary Sciences, Macau University of Science and Technology, Macau, China

[4]Centrum Badan Kosmicznych Polskiej Akademii Nauk (CBK PAN), PL-00–716 Warsaw, Bartycka, 18A, Poland

Key Points:

- HFR is an UWB SAR developed to retrieve the 3D structure of the first ten meters of an asteroid's subsurface
- SAR Tomography (TomoSAR) is crucial to improve the resolution in the vertical direction.
- In the specific asteroid geometry, simulations are necessary the assess the performances of the TomoSAR algorithms.

Abstract

Our knowledge of the internal structure of asteroids is currently indirect and relies on inferences from remote sensing observations of surfaces. However, it is fundamental for understanding small bodies' history and for planetary defense missions. Radar observation of asteroids is the most mature technique available to characterize their inner structure, and Synthetic Aperture Radar Tomography (TomoSAR) allows 3D imaging by extending the synthetic aperture principle in the elevation direction. However, as the geometry of observation of small asteroids is complex, and TomoSAR studies have always been performed in the Earth observation geometry, TomoSAR results in a small body geometry must be simulated to assess the methods' performances. Different tomography algorithms can be adopted, depending on the characteristics of the problem. While the Frequency Domain Back Projection (FDBP) is based on the correction of the Fourier transform of the received signal by an *ad-hoc* function built from the geometry of study, it can only retrieve the true position of the scatterers when applied along with ray-tracing methods, which are unreliable in the case of rough asteroid surfaces. Meanwhile, the Compressive Sensing (CS) is based on the compressive sampling theory, which relies on the hypothesis that few scatterers lie in the same direction from the subsurface. The CS can be used to retrieve the position of the scatterers, but its application in the small body geometry is questioned. Thus, both performances of the FDBP and the CS in a small body geometry are demonstrated, and the quality of the reconstruction is analyzed.

1 Introduction

In standard high-resolution 2D SAR imaging, the spatial resolution along the slant-range direction is achieved by sending pulses with a wide bandwidth, and along the azimuth direction (along-track direction) by regularly sending pulses on a large synthetic aperture (Curlander & McDonough, 1991). However, because of the penetration of the waves, the returned echoes contain information about the surface under study as well as the subsurface and the resolution cell is spread in the 3rd direction of space, perpendicular to the line-of-sight direction and to the along-track direction. As the SAR image is a 2D mapping of the reflectivity of the scene, the resulting image is a projection of the reflectivities of the 3D volume to a 2D surface. Thus, image distortions may happen, such as layover, shadowing, or foreshortening, which degrade the 3D reconstruction of the scene and alter the imaged geometry. The 3rd direction of space is named hereafter elevation, even if some authors use this name to refer the range direction when projected on a 2D map.

Interferometric SAR (InSAR) (Ulander & Frolind, 1998) was first developed as an answer to this problem since it determines the height of a target by measuring the phase difference between several observations separated in space and/or in time. However, as the measured height is the height of the phase center of all the scatterers in the same range-azimuth cell, the position of each scatterer still cannot be resolved. Polarimetric SAR interferometry (Cloude & Papathanassiou 1998) was then developed and was used to separate between surface and volume scattering effects within the same resolution cell and estimate their associated heights. However, this technique remains limited because it recovers only the mean height of all backscattering contributions in the same, large resolution cell. 3D SAR synthesis can also be considered, however, there is no resolution in the third dimension when imaging a surface with a single orbit.

SAR tomography was thus developed to overcome these limits. Its objective is to extend the synthetic aperture principle applied in the azimuth direction to the elevation direction, using 2D SAR images acquired with different positions in elevation. In this way, SAR tomography allows the reconstruction of a scene reflectivity profile along the elevation direction.

Since the first TomoSAR experiment (Reigber & Moreira, 2000), TomoSAR has received increasing attention and was applied to retrieve a forest's vertical structure (Cloude, 2007; Frey et al., 2008; Minh et al. 2016) or to reveal the inner structure of snowpacks (Frey et al., 2015), using its high-resolution capabilities. With the availability of SAR data with a high resolution, such as TerraSAR-X or COSMOS Skymes, high-resolution SAR tomography of urban areas began to be developed (Lombardini et al., 2009; Zhu & Bamler, 2010). Besides, in the recent years, radar detections have been successfully performed to probe into planetary bodies' subsurfaces, such as the Moon (Nozette et al., 2010), Mars (Seu et al., 2007; Picardi et al., 2005), and on comets (Kofman et al., 2015). However, until now, all TomoSAR experiments have been conducting for large planetary surfaces but never applied to the smaller, kilometric bodies of our solar system.
The radar HFR - High-Frequency Radar - was developed in the frame of the AIDA/AIM mission (Herique et al., 2019b; Michel et al 2016) to investigate the shallow subsurface of a kilometric asteroid with a sub-metric resolution, and TomoSAR algorithms are considered to improve the instrument's resolution in the elevation direction. However, as the geometry of observation of a small, kilometric body with HFR has several major differences with the Earth observation geometry, the applicability of tomography algorithms is questioned.
This paper presents the results of the application of the Frequency Domain Back Projection (FDBP) and the Compressive Sensing (CS) TomoSAR algorithms on simulated SAR data obtained in an asteroid observation geometry. First, the characteristics of the observation of a small asteroid with HFR are presented, and the necessities of simulating the performances of TomoSAR algorithms in this geometry are highlighted. Then, different TomoSAR algorithms are described and the results of the FDBP are presented. Finally, the interests of CS for a small asteroid are presented, the method is implemented to improve the localization of an inclusion in the asteroid's subsurface, and its results are compared with those obtained by FDBP.

2 Radar observation of small bodies from orbit

Ultra-wideband tomography of kilometric asteroids is one of the key techniques to probe their inner structure. To better understand the stakes of the measurement, we present here the mission AIM (ESA) which boarded the High-Frequency Radar (HFR), designed for the specific observation of kilometric asteroids.

2.1 AIM and HFR

In the frame of the mission AIDA (Asteroid Impact and Deflection Assessment), NASA's DART (Double Asteroid Redirection Test, Cheng et al., 2012), is a kinetic impactor designed to impact the moon of the binary asteroid (65803) Didymos, while ESA's AIM (Asteroid Impact Mission, Michel et al., 2016) was developed for its phase A/B1 to observe the asteroid structure state before and after the impact. The mission AIM was proposed to the ESA council 2016 –but was unfortunately not funded- to be launched in 2020 and reach Didymos in 2022.
Didymos is an S-type binary asteroid, consisting of a main body which is about 800 meters large, and its moon, which is about 10 meters large. A preliminary shape model was derived using observations from Arecibo and Goldstone radars and photometric data.
Because of its small size, and thus mass, Didymos is supposed to have a weak gravity field. Its rotation period is slightly higher than 2.2 hours, which is just above the limit of disruption for kilometric asteroids (Walsh & Richardson, 2008) and makes it a probable rubble pile. To fulfill its

objectives, AIM boarded HFR to probe the asteroid's shallow subsurface, identify layerings, and to link different surface measurements to the subsurface structure.

HFR (Herique et al., 2018, 2019b) is a monostatic ultra-wideband, step frequency SAR, derived from the radar WISDOM (Ciarletti et al., 2017). This radar operates with frequencies ranging from 300 MHz to 800 MHz in nominal mode and up to 3 GHz in an optional mode. HFR's frequencies are a trade-off between penetration depth, range resolution, and technical constraints, especially the antenna size (Herique et al., 2019a,b). Indeed, a deep investigation requires low frequencies to reduce the dielectric and scattering losses, whereas subsurface probing requires a high resolution, achieved with a wide band, and thus high frequencies. HFR's band of 300-800 MHz allows probing the top ten meters of the asteroid subsurface with a resolution in the range direction better than one meter, while the 3 GHz mode allows probing the surface with a higher horizontal resolution.

As an ultra-wideband radar studying a kilometric asteroid, HFR has major differences with classical radars, such as the ones used in the space-borne Earth observation. These differences are highlighted by considering HFR's scenarios of observation with AIM.

2.2 Scenarios of observation

In a small body geometry, the motion of the radar with regard to a target on the asteroid is dominated by the rotation of the asteroid itself while the spacecraft is considered motionless in an inertial frame: a point at the surface is then observed from its "rise" at the horizon until it is disappearing, with a relative velocity of less than 1 m per second.
To analyze the specificities of the small body observation, we consider a sequence of AIM observed as planned by ESA, computed using the NASA/SPICE library (https://naif.jpl.nasa.gov/naif/toolkit.html). The AIM spacecraft is motionless in an inertial frame at a distance of about 12 km from the asteroid's mass center. All computations and visualizations will be presented in a rotating frame linked and centered on the asteroid. After 30 minutes of observation, the spacecraft's trajectory is presented in this frame in Figure 1, bottom, where the geometry's changes are dominated by the asteroid rotation.

This geometry of observation of Didymos with HFR has several major differences with the Earth observation geometry:

- While in Earth observation, the radar's trajectory can be considered as rectilinear during the illumination time, in the observation of Didymos with HFR, the trajectory is dominated by the Didymos' rotation, as presented in Figure 1.
- For Earth-observing radars, the surface observed by a radar can be considered planar in a first approximation due to the narrow antenna pattern. However, HFR's antenna beam covers the whole observed body, and the hypothesis of a plane surface for Didymos does not stand.
- HFR is an ultra-wideband radar, which means that its band Δf is not negligible to its central frequency f_c : $\frac{\Delta f}{f_c}$ =0.91. The radar's wavelength almost triples during the observation, from 0.375 m to 1 m.

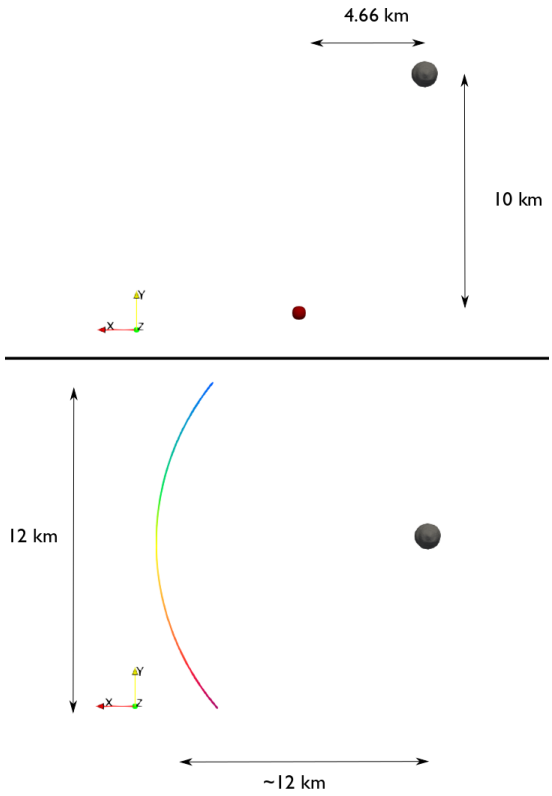

Figure 1. HFR's orbitography. The radar antenna (red dot) is motionless in an inertial frame (top) at the position [4.66,-10.0,5.77], while the asteroid (gray sphere) is moving. In a frame linked to the asteroid (bottom), the radar apparent motion is due to the asteroid rotation, while the asteroid is motionless. Red depicts the beginning of the trajectory and blue the end.

- Earth-observing radars observe surfaces at distances sufficiently large to consider that the slant range distance between the spacecraft and a given point of the scene is close to being constant during the entire observation. The same assumption can often be laid on the incidence angles when the observation time is sufficiently short. However, the geometry of the observation of Didymos is dominated by the body's rotation, and the whole asteroid is seen by HFR's antenna beam. Thus, the incidence angles and the slant-range distance cannot be easily approximated, and the range migration cannot be compensated.

Thus, classical hypotheses usually formulated for stripmap SAR in the Earth observation may not stand in the observation of small bodies, and the end-to-end performances of a given scenario can be evaluated from simulation only. Only in this way any data-processing algorithms can be validated. Namely, since the range/Doppler separability cannot be assumed in this geometry, the SAR processing applied in our simulation is called "brute-force" and compensates the range and Doppler delays all-together. With all of these differences, the classical point target pattern shaped as a product of two cardinal sines in the Earth observation geometry (Figure 2, top) is not retrieved in the observation of Didymos and will depend on the scenario of observation and the radar's characteristics. In the case of our simulation, the point target pattern acquires a "star-like" shape, as presented in Figure 2 (bottom).

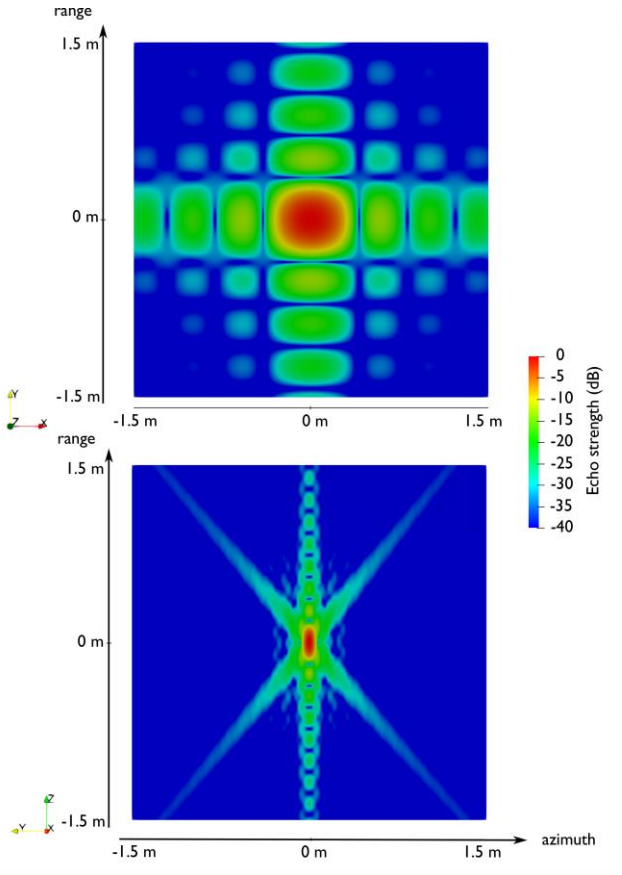

Figure 2. Examples of point target patterns. In the Earth observation geometry, the pattern will have the classical shape of a product of cardinal sines in the range and the Doppler directions (top). The point target pattern in an asteroid observation geometry (bottom) will depend on the geometry of observation and the radar characteristics and is shaped like a star in the observation of Didymos. The results are depicted with a 40-dB range dynamic normalized to the maximum power.

HFR aims not only at studying the surface, but the subsurface as well of small bodies, with a metric resolution in the third direction of space, the elevation direction. In order to compute this resolution, 3D SAR syntheses are necessary.

2.3 3D SAR Synthesis

Using the scenario of observation described previously and computing the spectrum scattered by a point target, the 3D SAR synthesis of a target located at [0°, 0°] latitude and longitude on the surface of the asteroid was performed. The signal was simulated using the SPRATS toolbox, designed to simulate and interpret radar data in the frame of space mission analysis and preparation of spatial operations (Gassot et al., 2020). The synthesis is carried out using the FDBP algorithm, described by Soumekh et al. (1999), which is based on the compensation of the phase of each scatterer during the observation.

The SAR synthesis is processed on a volume large of $5 \times 5 \times 5\ m^3$ and is pictured in Figure 3, where the point target position is indicated by a white sphere in Figure 3. On the SAR image, high power is associated along the elevation direction. This feature is called the elevation ambiguity.

This ambiguity is an expected feature on spherical bodies when only one track is flown and illustrates that the target position in elevation is ambiguous. The elevation ambiguity is shaped like a straight tube in the Earth observation geometry but is shaped like an “hourglass” in the Didymos observation geometry. Indeed, as the trajectory is dominated by the asteroid rotation, it is not rectilinear and explores a few different elevation positions in the 3D domain. This allows focusing the target and explains why the target is imaged with a resolution in the elevation direction. As the trajectory is not aligned with the equatorial plane of Didymos, the ambiguity is defocused at all points in space, except at the position of the target. By measuring the width of the 3 dB spot presented in Figure 3 (presented as a bright red shape) the resulting elevation resolution is computed to be 2.2 m with a single-track orbit, while the range resolution is 54 cm due to the 500 MHz bandwidth and the incidence of about 30°, and 21 cm in Doppler due to the 30 min

observation duration. The elevation resolution is thus much poorer than the azimuth and range resolution and is not sufficient to probe the first tens meters of the subsurface.

HFR is a new instrument dedicated to the UWB study of asteroids, designed to probe an asteroid subsurface with a sub-metric resolution. However, any SAR observing a surface will have no resolution in the third direction with a single orbit. Since HFR’s orbit is not rectilinear, the radar’s trajectory will explore lightly the third direction (the elevation direction), and the resolution in the elevation direct would exist but would be too poor to comply with the objectives of HFR to probe an asteroid with a resolution of less than 1 m in the vertical direction. Tomography algorithms are a solution to improve the elevation resolution and probe the subsurface with a decimetric resolution.

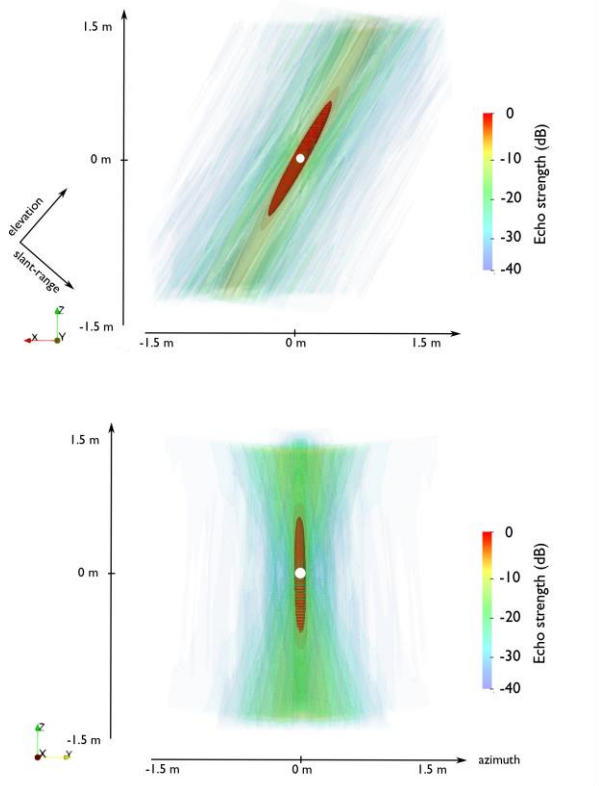

Figure 3. 3D SAR synthesis results from the front (top) and the side (bottom) with a dynamic of 40 dB normalized to the maximum power. The white sphere shows the theoretical position of the target. The 3 dB portion is pictured as bright red.

3 SAR Tomography

TomoSAR algorithms have been developed to recover the 3D structure of embedded objects or reconstruct anthropic structures in urban areas. Since a large variety of algorithms exist, they are reviewed and classified, and the most fitted TomoSAR algorithm is selected.

TomoSAR algorithms can be classified into three main families:

1) Traditional 2D SAR imaging algorithms applied in the 3D domain.
   They can be organized into frequency and time domain algorithms:
   - The frequency-domain methods, such as the SPECAN (SPECtral ANalysis, Reigber & Moreira, 2000), operate a Fourier transform to focus the received signal along the elevation direction. Their main appeal is their low computational burden. However, it is challenging to observe a scene with evenly distributed flight tracks: because the received data are always undersampled due to the small number of observations, an additional interpolation procedure is always needed, which increases the computational burden and reduces the interest of these methods. However, the method cannot be applied when the range migration caused by the multiple orbits exceeds half the resolution cell.
   - The time-domain methods, such as the TDBP (Time-Domain Back Projection) method (Nannini et al., 2006) directly focus the signal in elevation with an ad hoc function. These methods do not rely on a regular distribution of flight tracks. However, they are time-consuming. The TDBP can be expressed in the frequency-domain, and is then called FDBP (Frequency Domain Back Projection, Soumekh, 1999).

2) The Polarimetry Coherence Tomography (PCT).
   This method uses POLInSAR data to derive the elevation reflectivity function, characterized by the Fourier Legendre series. Using a single or dual baseline architecture, the PCT method has been implemented to derive the elevation profile of the radar scattering intensity, while avoiding any flight track control (Cloude, 2006). However, PCT relies on a priori knowledge on the height of the scattering volume and the phase of the ground, which adds some additional procedures when this knowledge is not available and increases its computational load. Finally, due to the small number of baselines, the spatial resolution of the PCT tomogram is not as good as different tomography methods.

3) The Spectral Estimation (SE) methods.
   These methods are high-resolution TomoSAR algorithms, which are based on an inversion problem between the measurement vector and a matrix called the mapping matrix to retrieve the vector reflectivity profile. They can be classified as parametric or non-parametric models:
   - Parametric models, such as the MUSIC (MUltiple SIgnal Classification) algorithm (Nannini et al., 2011) are easily implemented but require a priori information on the surface to be imaged, such as the number of scatterers.

- Non-parametric models, such as the CS (Compressive Sensing) algorithm (Zhu & Bamler, 2010) are more flexibles but rely on hypotheses on the investigated geometry that may be hard to satisfy.

However, the SE methods cannot be applied when the range migration caused by the multiple orbits exceeds half the resolution cell.

Ultimately, the choice of one model instead of another relies on the characteristics and requirements of the study, since each of these models has its advantages and drawbacks. Table 1, which is built from the description of each model, classifies the different methods depending on their computational burden, their resulting spatial resolution, the operation complexity (the difficulty to carry on the observation in a nominal way), and the adaptability of the algorithm to correct the delay induced by the permittivity of the subsurface.
Given the high resolution provided by the radar, the range migration caused by the different orbits will exceed half the resolution cell size in our scenario, which excludes frequency domain methods as well as spectral estimation methods for a correct reconstruction of the reflectivity profile. Since we applied the FDBP to compute the 2D SAR synthesis, its 3D-domain application a natural first choice to be applied in tomography.

3.1 Scenario of simulation

To validate the method and evaluate the performances, we first simulate a data set for a scenario of observation. We consider the signal backscattered by an inclusion embedded in the asteroid subsurface for several elevation incidences, which are described by the spacecraft's orbitography.

Our scenario of observation considers the orbit described in Section 2.2, repeated 20 times, with an offset of 500 m between each track. The resulting geometry of observation is presented in Figure 4.
We consider an inclusion located at 25 cm under the asteroid surface. The surface is modeled as a $50\times50\text{-cm}^2$ large mesh of 20×20 point facets with a constant permittivity of 3.0, the permittivity of dry sand, which is similar to the texture expected from rocky asteroids surfaces (Herique et al., 2019a). The inclusion is modeled with a permittivity of 3.1, embedded in a subsurface, associated with a permittivity of 3.0.

Table 1. TomoSAR algorithms performances

	Computational burden	Spatial resolution	Complexity	Adaptability to a change of ε
SPECAN	Medium	Medium	High	Low
FDBP	High	Medium	Medium	Low
PCT	Low	Low	Low	Medium
CS	Medium	High	Medium	Medium

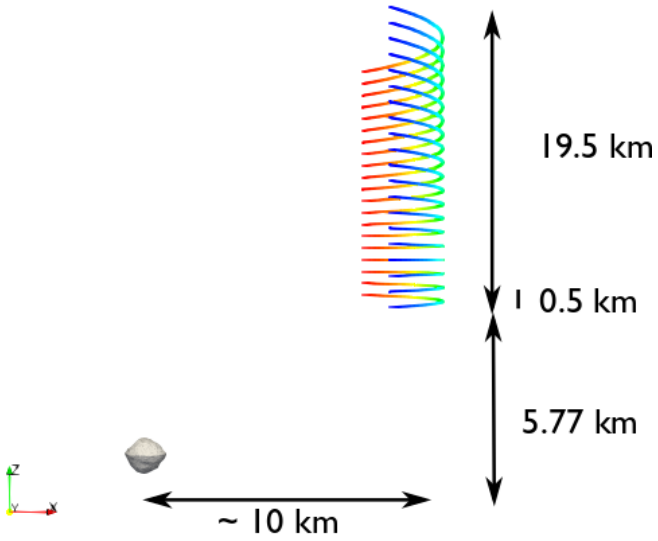

Figure 4. The 20 trajectories used for the TomoSAR algorithms. This view is in a Didymos centered frame. The red part pictures the beginning of the trajectory and the blue the end.

The spectrum scattered by the surface is computed using the facet method, which estimates the field scattered by each facet by applying the Fresnel coefficients and computes the facet's scattering lobe. The facet method was implemented using SurfaceEchoPO (Nouvel et al., 2005, Berquin et al., 2015).

The field transmitted by the surface to the inclusion is computed with the facet method as well, while the field backscattered by each inclusion is computed using the Born Approximation (Ulaby et al., 1986). The method considers that the field inside a volume of average permittivity ε_a , perturbed by different inclusions of permittivity ε_f, is equal to the field that would be present without the inclusions. Then, the field scattered by each inclusion can then computed from the field inside the volume. This approximation is valid only if the contrast in the dielectric permittivity between the inclusion and subsurface $\Delta\varepsilon$ is small. In our scenario, $\varepsilon_a = 3.0$ and $\Delta\varepsilon$ =0.1. The parameters of the simulation are summarized in Table 2.

Before presenting the TomoSAR results of the scenario, one should note that the simulations of the scattered spectrum do not cover any process gain, antenna gain, or synthesis gain. Moreover, they do not consider any gain that may be reached with the range/Doppler compression. By additionally considering the very small size of the volume understudy, in the end, the power of the scattered spectrum will be very low. However, the goal of this study is to validate the reconstruction of an inclusion with TomoSAR, and not to estimate its behavior in a physical, realistic scenario. This would be performed in further studies once the behavior of the TomoSAR in a small body geometry is validated.

3.2 Application of the TomoSAR FDBP

3.2.1 Description of the TomoSAR FDBP

The FDBP is presented in 2D imaging in Soumekh et al., (1999) and achieves focusing by using the geometry between the sensor and the imaged volume: every resolution cell of the 3D SAR image is focused based on the true acquisition geometry and a reference function. The TomoSAR FDBP is based on the same principle and considers 3D SAR images $s_n(\vec{r_l})$, already focused on the range/doppler plan. For each track, the image s_n corresponds to the n-th flight track :

$$s_n(\vec{r_l}) = \sum_{j=a_n}^{b_n} S(f_m) \cdot \exp\left(i4\pi f_m \frac{R_{n_{ij}}}{c}\right) \quad (1)$$

With:

S: the measured spectrum
$\vec{r_l}$: the position of the scatterer
a_n, b_n: the indexes of the first and last azimuth position of the sensor
$\overrightarrow{r_{s_{jn}}}$: the position vector of the sensor of the n-th track
$R_{n_{ij}} = \left|\vec{r_l} - \overrightarrow{r_{s_{jn}}}\right|$: the range distance
f_m : the frequency.

The TomoSAR image v is then the sum of all spectra for all tracks and can be written at the position $\vec{r_l}$:

$$v(\vec{r_l}) = \sum_{n=1}^{N} \sum_{j=a_n}^{b_n} S(f_m) \cdot \exp\left(i4\pi f_m \frac{R_{n_{ij}}}{c}\right) \quad (2)$$

As a TomoSAR algorithm, the resolution expected from FDBP can be obtained by (Reigber & Moreira, 2000):

$$\delta_e = \frac{\lambda r_0}{2L} \quad (3)$$

Where λ is the wavelength, r_0 is the range distance, and L the distance covered by all trajectories in the elevation direction. Considering that L = 8.33 km in our scenario, the expected resolution was computed to be 39 cm.

3.2.2 Numerical Results

The FDBP was applied to our scenario and its result is presented in Figure 5, with the position of the target highlighted by a white sphere. The elevation resolution achieved with the multipass geometry is improved from 2.2 m and reaches 47 cm, which is comparable to the 39 cm theoretical resolution expected from TomoSAR algorithms. The theoretical resolution is not reached because its expression was carried out in the Earth observation geometry and not in our specific small body

Table 2: Simulation parameters

Radar central frequency	550 MHz
Radar bandwidth	500 MHz
PRF	0.12 Hz
Surface size	50 cm
Surface Sampling	2 cm
Inclusion size	0.5 cm
Volume permittivity	3.0
Inclusion permittivity	3.1

geometry. However, the position of the target cannot be retrieved by the FDBP. Indeed the SAR processor has no knowledge of the medium permittivity, and the position of the target is then shifted.

Traditionally, ray tracing methods are implemented to correct the delay induced by the propagation of the wave in a medium where the permittivity is different from 1.0. However, these methods are highly dependent on the shape models. Given the very rough surfaces of asteroids, ray tracing methods are not reliable in the small body geometry and will not be considered.

3.3 Reconstructing the true position of the target with the Compressive Sensing

To reconstruct the true position of the target, additional tomography methods can be considered. The Compressive Sensing (CS) is a spectral estimation method based on the computation of SAR images of the surface of the volume investigated, and on the retrieval of the reflectivity profile in the elevation direction if this reflectivity profile is sparse. This means that the CS treats the propagation of the waves in the void (by computing the SAR image at the surface) and the subsurface (by computing the reflectivity profile of the subsurface) separately. Thus, the compensation of the delay can be carried out more easily than by correcting the SAR processing. However, the CS is not entirely adapted in a geometry where the range migration exceeds the size

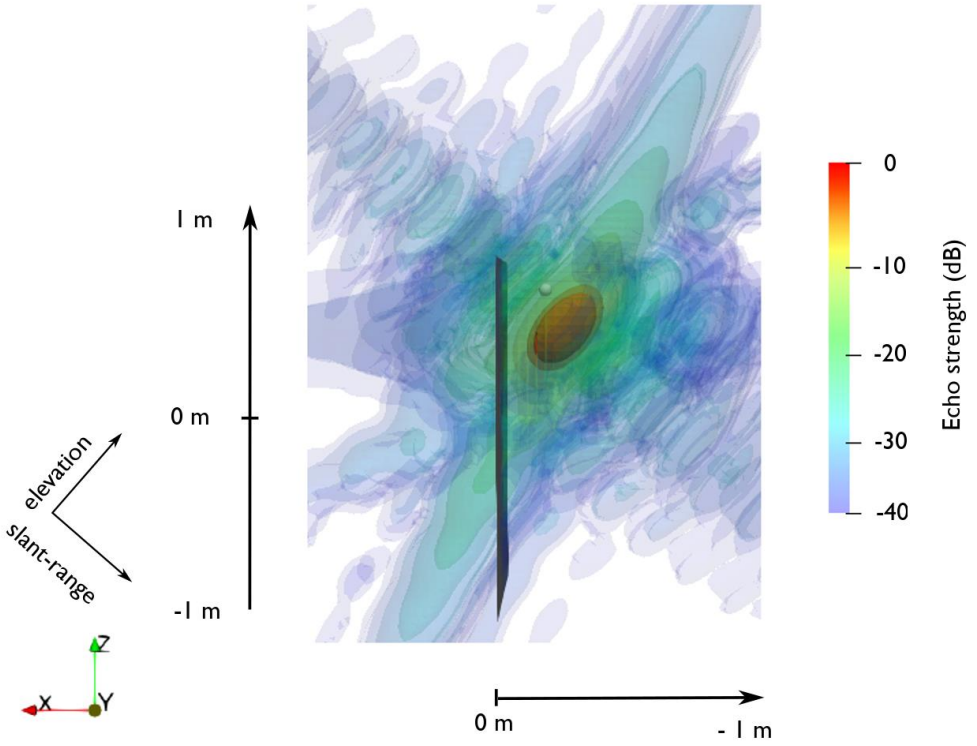

Figure 5. FDBP TomoSAR results with a dynamic of 40 dB normalized to the maximum power. The white sphere pictures the theoretical position of the target, and the surface is represented to help visualize the geometry. The 3-dB portion is pictured as bright red.

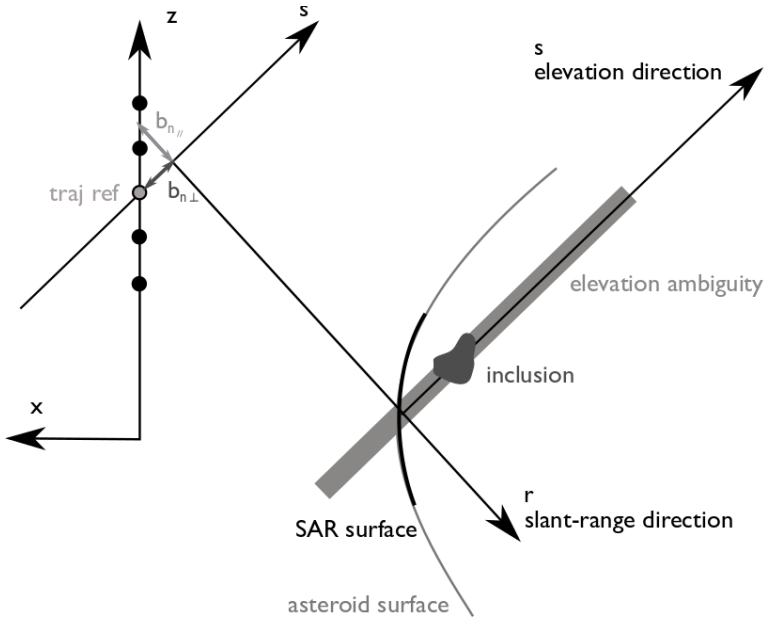

Figure 6. Compressive Sensing geometry in a small body geometry probing a single inclusion in the subsurface of an asteroid. The different tracks are represented as black spots in the z-direction, and the reference track is highlighted. s depicts the elevation direction and r the range direction

of the resolution cell, which is the case in our small body geometry. As a consequence, the performances of the CS will deviate from the nominal performances and will not be as high as the performances achieved with the FDBP. Nevertheless, by treating the propagation of the wave in two steps, in the void and the subsurface, the CS can be applied to retrieve the true position of the scatterers.

3.3.1 TomoSAR using Compressive Sensing

In a multipass SAR acquisition, the value of a SAR pixel g located at the position (x, r) corresponds to the integral of the reflected signal along the elevation direction:

$$g_n(\mathrm{x},\mathrm{r}) = \int_s \gamma(x,r,s)\exp(-\tfrac{4j\pi}{\lambda} d_n(x,r,s))ds \quad (4)$$

With n indicating the position of the pass in a multipass geometry, s is the elevation position, γ is the pixel's reflectivity, d_n is the distance from the radar to each pixel and λ is the wavelength. Following the derivation developed by Fornaro et al. (2003), which was carried out in the Earth observation geometry, by defining a reference track, we find that :

$$g_n(\mathrm{x},\mathrm{r}) = \int_s \gamma(s)\exp\left(2j\pi \tfrac{2}{\lambda}\tfrac{b_{n\perp}}{(r-b_{n\parallel})}\right)ds \quad (5)$$

Where $\gamma(x,r,s)$ is written γ for simplicity, r is the slant range distance between the surface and the reference track and $b_{n\perp}$ and $b_{n\parallel}$ are the parallel and orthogonal distances between each track and the reference track, as presented in Figure 6.

Thus, by discretizing the continuous elevation function s, we can write:

$$\boldsymbol{g} = \mathrm{R}\boldsymbol{\gamma} \quad (6)$$

Where g is the measurement vector, γ is the elevation reflectivity profile vector, and R is a matrix called the mapping matrix, expressed as:

$$R_{nl} = \exp\left(-2j\pi \cdot \tfrac{f_n}{c} \cdot s_l\right) \quad (7)$$

With :

$$f_n = -2f \cdot \tfrac{b_{n\perp}}{(r-b_{n\parallel})} \quad (8)$$

Where s_l depicts the discretization of the elevation vector and f is the central frequency of the signal.

The objective of TomoSAR is to retrieve the elevation profile $\gamma(s)$ for each azimuth-range pixel (x, r), which is performed by an L1-norm minimization:

$$\hat{\boldsymbol{\gamma}} = \arg\min\{\|\boldsymbol{\gamma}\|_1\} \quad s.t \;\; \boldsymbol{g} = R\boldsymbol{\gamma} \quad (9)$$

This minimization can be easily achieved with basis pursuit methods (Van den Berg & Friedlander, 2011).

3.3.2 Correction of the delay

One of the main attractions of the Compressive Sensing is its potential to correct the delay induced by the propagation of the wave in the subsurface. The compensation of the delay of the signal can be understood by considering a target embedded under a surface. Because the SAR processor considers that the signal is always propagating in the void, the final SAR image sees any point below the surface located deeper than it actually is. This means that the elevation ambiguity in the void and in the subsurface will not have the same orientation, yet the SAR processor will consider the elevation ambiguity has always the orientation of the void's. Thus, as illustrated in Figure 7, targets lying at an angle θ_2 from the point on the surface with the same range/azimuth delay, will be imaged at an angle θ_1.

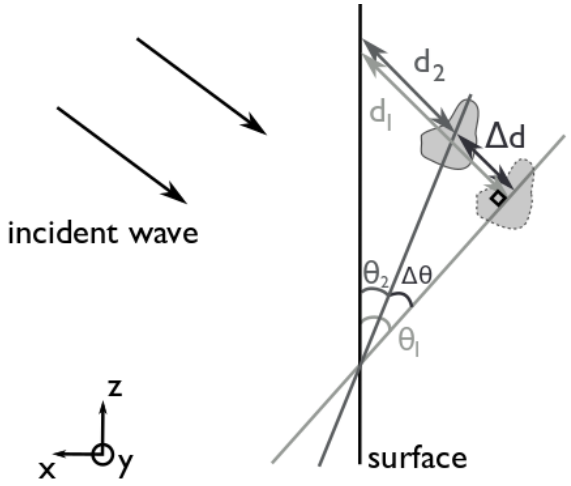

Figure 7. Illustration of the measurement error induced by the permittivity of the medium. A target embedded at a distance d_2 from the surface will be imaged at a distance d_1.

As the CS aims at retrieving all scatterers in the elevation direction, the compensation of the delay can be carried out by first retrieving all scatterers on the elevation profile, computed in the void and then performing a rotation by an angle $\Delta\theta$ and a dilatation of parameter $\frac{1}{\cos(\Delta\theta)}$, to retrieve the actual elevation profile in the medium, with:

$$\Delta\theta = \theta_2 - \theta_1 = \operatorname{atan}\left(\left(1 - \frac{1}{\sqrt{\varepsilon_a}}\right) \cdot \tan(\theta_1)\right) \quad (10)$$

3.3.3. Numerical results

20 2D SAR images of the scenario described in section 3.1.2 were computed at the surface of the asteroid, and the CS method was then implemented with a basis pursuit method algorithm, using the SPGL1 algorithm with the SPGL1 python library (van der Berg & Friedlander, 2007). For each

pixel of the SAR image, the reflectivity profile γ was retrieved on an elevation profile 3 m in length, with a sampling of 3 cm. First, the CS results without the compensation of the delay are presented in Figure 8, top, with a dynamic range of 40 dB, where the 3-dB portion which indicates the retrieved position of the target. The theoretical position of the target is indicated with a white sphere.

The difference between the position of the located target and its theoretical position is due to the delay produced by the permittivity of 3.0, and is expected since no compensation of the delay was performed. No sidelobes appear in the range or doppler dimensions since they are taken into account in the reflectivity model. The CS achieves an elevation resolution of 60 cm, which is worse than the 47 cm resolution achieved with the FDBP, as presented in Table 3. This difference is expected since the conditions of the application of the CS are not fully retrieved in our geometry.

However, the CS was then applied with the correction of the delay, and the results are presented in Figure 8, bottom. As expected, the compensation of the delay improves the localization of the target, which falls into the 3-dB width spot, with a resolution of 61 cm. The comparison of the resolution achieved with the different methods are presented in Table 3. Further differences between the localization of the target and its true position may be due to additional refraction effects.

As the CS is performed starting from a stack of SAR images using the Born Approximation, the CS limits are linked to the Born Approximation limits. Indeed, the asteroid's surface is described as a mesh of facets. To keep the far-field hypothesis correct for all inclusions in the sub-surface, the facets must be designed small enough to behave a point targets, which requires a large sampling and thus causes long computation times. Further improvement will have to be carried out on the Born Approximation to reduce the computation time, in order to test the CS with scenarios with a larger number of inclusions or larger volumes, which could be used to further validate the model.

Table 3. Comparison of the resolution achieved with a single pass SAR synthesis, with the Compressive Sensing, and the theoretical expected value.

	Single-pass	Theoretical (TomoSAR)	Multi-pass synthesis	CS
Resolution (m)	2.2	0.39	0.47	0.6

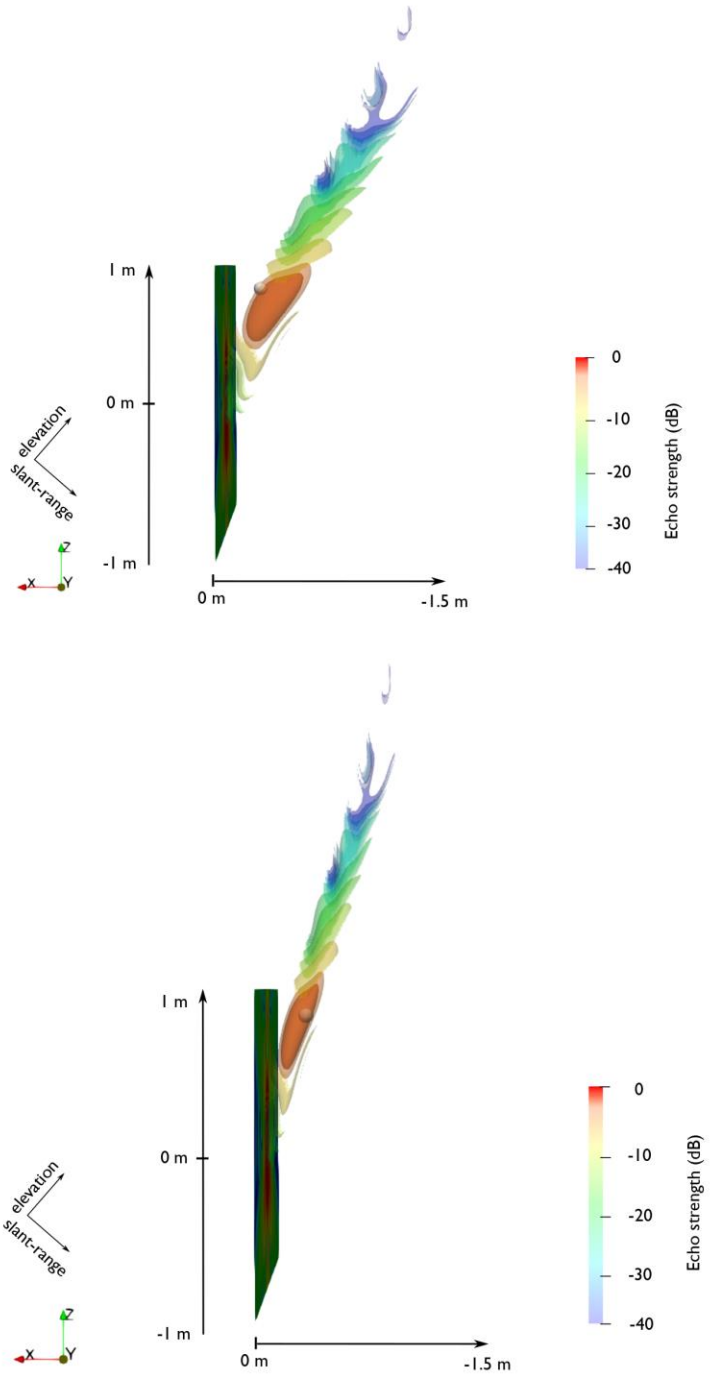

Figure 8. (Top) Compressive Sensing results with a dynamic of 40 dB normalized to the maximum power, considering that the target is located in the void. The white sphere indicates the theoretical target position and the reflectivity 3-dB portion is indicated by the bright red section. (Bottom) Compressive Sensing results with a dynamic of 40 dB normalized to the maximum power by compensating the phase delay, considering that the target is located in a medium with a permittivity of 3.0. The white sphere indicates the theoretical target position and the reflectivity 3-dB portion is indicated by the bright red section.

4 Conclusions

The UWB radar HFR was developed to observe the first ten meters of asteroids' subsurface, with a sub-metric resolution. To improve the resolution in elevation, tomography methods can be carried out. We present in this paper how the Frequency-Domain Back-Projection method (FDBP) TomoSAR is implemented in a small body geometry and images a single embedded inclusion with a resolution of 47 cm. However the method cannot reconstruct the position of the inclusion when the permittivity of the subsurface is different than one, and the ray-tracing methods which could be applied to correct the position is unreliable in the small body geometry. The compressive sensing (CS) method can be applied to overcome this limitation. If we model the asteroid subsurface as consisting of few point-like scatterers, the reflectivity profile of each point of the asteroid surface is sparse, and thus the CS can be applied. The CS method consists of an L1-norm minimization and was applied to the reconstruction of scatterers in urban areas (Zhu & Balmer, 2010). However, it was never applied in an asteroid geometry and the fact that range migration is higher than the resolution cell size invalidates its application. Nevertheless, the CS allows improving the localization of the target with the knowledge of the medium permittivity. We presented in this paper how the CS was applied in the small body geometry. The resolution retrieved by the CS is worse than the resolution retrieved by the FDBP, which is expected since the hypotheses of the application of the CS are not retrieved, but the CS manages to retrieve the position of the scatterer.
The CS cannot yet be tested with several targets because of computational limitations with our current volume scattering model, the Born Approximation. Different works are under study to overcome these limitations and would be needed to test the performances of CS to distinguish between closely separated scatterers.

Even though the mission AIM was not funded in 2016, the mission Hera (Michel et al., 2018) is an updated version of AIM. On Hera, the small Juventas will board JuRa –Juventas Radar- , a low frequency monostatic radar with frequencies ranging from 50 MHz to 70 MHz to study the inner structure of Didymos (Herique et al., 2019a). Hera and JuRa will benefit from the results of the applicability and the performances of the CS on the Didymos geometry, since the observation geometry stays the same, despite the change of frequencies, and thus, of resolution.
Further work on the CS application will focus on overcoming the Born Approximation limitations, and simulate the behavior of several pointlike targets, as well as several larger targets and test the CS performances.

Acknowledgements

Hera is the ESA contribution to the AIDA collaboration.
Juventas and JuRa are developed under ESA contract supported by national agencies.
JuRa is built by Emtronix (Lux), UGA/IPAG (Fr), TUD (Gr), Astronika (Pl) and BUT (Cz).
Juventas is built by Gomspace (Lux).
This work has been supported by ESA's General Studies Program (AIM Phase A and UWBTO study).

The code described in this paper is described in Kong et al., (2000) for the facet method, Soumekh. M, (1999) for the FDBP and Zhu & Bamler, (2010) for the CS. The scripts and resulting data used for supporting the figure results can be found in :
Gassot et al., 2020, Ultra-wideband SAR Tomography on asteroids : FDBP and Compressive Sensing datasets, Version 1. Aug 2020, Univ. Grenoble Alpes, CNRS, CNES, IPAG, 38000 Grenoble, France. https://doi.org/10.5281/zenodo.3981252. Accessed 2020-08-12.

Appendix

Compressive sampling

Compressive sampling is a technique adapted to the reconstruction of sparse signals, described in [28]. A signal x of length L is said K-sparse in an orthogonal basis ψ if the projection of x onto ψ, $\boldsymbol{s} = \psi\boldsymbol{x}$ has only K non-zero elements.
If a measurement vector of size N s is obtained by projecting $\boldsymbol{x}$ onto a matrix Φ, where Φ is called the sensing matrix, then we can write:

$$\mathbf{y} = \Phi\,\boldsymbol{x} = \Phi\,\psi^{H}\boldsymbol{s} = \Theta\boldsymbol{s} \tag{A1}$$

Where Θ is called the mapping matrix, and H stands for the conjugate transpose operator.
Using the compressive sampling method, s can be reconstructed by L_0-norm minimization, which finds the solution of equation (1) with the minimum number of non-zero coefficients:

$$\hat{\boldsymbol{s}} = \arg\min\{\|\boldsymbol{s}\|_0\} \quad \text{s.t } \boldsymbol{y} = \Theta\boldsymbol{s} \tag{A2}$$

For sparse signals, the L_0-norm minimization and the L_1-norm minimization leads to the same results. Thus, s can be found using the L_1-norm minimization:

$$\hat{\boldsymbol{s}} = \arg\min\{\|\boldsymbol{s}\|_1\} \quad \text{s.t } \boldsymbol{y} = \Theta\boldsymbol{s} \tag{A3}$$

This minimization can be performed using basis pursuit methods [29]. To have a unique solution, two conditions must hold:

- The sensing matrix Φ and the orthogonal basis ψ must be incoherent, in order not to bias the reconstruction of non-zero elements into certain positions. The incoherence can be computed as :

$$\mu(\Phi,\psi) = \sqrt{n}\cdot\max\left|<\Phi_k\psi_j>\right| \qquad 1 < k,j < n \tag{A4}$$

Where n depicts the number of columns of Φ and ψ, k and j depict the index of the col

- The mapping matrix Θ must follow the Restricted Isometry Property (RIP), which guarantees a sufficiently sparse reconstruction in the presence of noise :

$$(1-\delta_s)\|\boldsymbol{v}\|_2^{\,2} \le \|\Theta\boldsymbol{v}\|_2^{\,2} \le (1+\delta_s)\|\boldsymbol{v}\|_2^{\,2}$$

Where $\boldsymbol{v}$ is any K-sparse vector, with non-zero coefficients at the same position as s, and δ_s is a small number. The smaller δ_s the better the sparse signal will be reconstructed in the presence of noise. This property assures that Θ preserves approximately the Euclidean length of the sparse signals. This implies that these vectors cannot be in the null space of Θ and can thus always be recovered and that all distances between sparse signals will be reconstructed in the measurement space.

Before applying the compressive sensing, these two conditions must thus be verified.

TomoSAR using CS

The Compressive Sensing method applied to TomoSAR imagery seeks to solve:

$$\hat{\gamma} = \arg\min\{ \|\gamma\|_1 \} \quad s.t \;\; g = R\gamma \tag{A5}$$

Where γ the reflectivity profile, g is the SAR image pixel, and R and a matrix composed of factors computed from the distance between the spacecraft and the surface.
However, to apply CS, three conditions must be verified:

- The signal γ is sparse. Considering only a few inclusions lie in each elevation direction of each SAR pixel, we can consider γ being sparse. As only one inclusion is considered, the sparsity of the signal is assumed.
- The orthogonal basis matrix ψ is the identity matrix in our geometry. As the distance between the radar to each SAR pixel is large considering the wavelength, the R matrix can be considered as random. R and ψ are thus incoherent.
- The RIP property is verified: In the case of a single scatterer, the RIP property is automatically verified. When imaging several scatterers, the RIP is verified if the scatterers are separated by a distance larger than the resolution (Zhu & Bamler, 2010)

As all CS hypotheses are validated, the CS can be applied to our study.

References

Berquin, Y., Herique, A., Kofman, W., & Eggy, E. (2015). Computing low-frequency radar surface echoes for planetary radar using Huygens-Fresnel's principle. *Radio Science*, *50*(10), 1097-1109

Cheng, A. F., *et al.* (2012). Dart: Double asteroid redirection test. In *European Planetary Science Congress* (Vol. 7, pp. 23-28)

Ciarletti, V. *et al.* (2017). The WISDOM radar: Unveiling the subsurface beneath the ExoMars Rover and identifying the best locations for drilling. *Astrobiology*, *17*(6-7), 565-584

Cloude, S. R., & Papathanassiou, K. P. (1998). Polarimetric SAR interferometry, *IEEE Transactions on geoscience and remote sensing,* 36(5), 1551-1565

Cloude, S. R. (2006), Polarization coherence tomography. *Radio Science*, *41*(4)

Cloude, S. R. (2007). Dual-baseline coherence tomography. *IEEE Geoscience and Remote Sensing Letters*, *4*(1), 127-131

Curlander, J. C, & McDonough, R. N. (1991). Synthetic Aperture Radar: Systems and Signal Processing, *Wiley series in remote sensing*.

Fornaro, G., Serafino, F., & Soldovieri, F. (2003). Three-dimensional focusing with multipass SAR data. *IEEE Transactions on Geoscience and Remote Sensing*, *41*(3), 507-517

Frey, O., Morsdorf, F., & Meier, E. (2008). Tomographic imaging of a forested area by airborne multi-baseline P-band SAR. *Sensors*, *8*(9), 5884-5896

Frey, O., Werner, C. L., & Wiesmann, A. (2015). Tomographic profiling of the structure of a snow pack at X-/Ku-Band using SnowScat in SAR mode. *2015 European Radar Conference (EuRAD) (pp. 21-24). IEEE*

Hérique, A. *et al*. (2018). Direct observations of asteroid interior and regolith structure: science measurement requirements. *Advances in Space Research*, *62*(8), 2141-2162

Gassot et al., (2020), SPRATS : a versatile Simulation and Processing RAdat ToolS for planetary miisions, accepted for IEEE radar conference.

Hérique, A. *et al*. (2019a). A Low Frequency Radar to Fathom Asteroids from Juventas Cubesat on HERA. *In 2019 EPSC-DPS Joint Meeting*

Hérique, A. *et al*. (2019b). A radar package for asteroid subsurface investigations: Implications of implementing and integration into the MASCOT nanoscale landing platform from science requirements to baseline design. *Acta Astronautica*, *156*, 317-329

Kofman, W. *et al.* (2015). Properties of the 67P/Churyumov-Gerasimenko interior revealed by CONSERT radar. *Science, 349(6247)*

Lombardini, F. *et al.* (2009). Linear and adaptive spaceborne three-dimensional SAR tomography: A comparison on real data . *IET radar, sonar & navigation*, *3*(4), 424-436

Michel, P. *et al.* (2016). Science case for the asteroid impact mission (AIM): a component of the asteroid impact & deflection assessment (AIDA) mission. *Advances in Space Research*, *57*(12), 2529-2547

Michel, P. *et al.* (2018). European component of the AIDA mission to a binary asteroid: Characterization and interpretation of the impact of the DART mission. *Advances in Space Research*, *62*(8), 2261-2272

Minh D.H.T. *et al.* (2016). SAR tomography for the retrieval of forest biomass and height: Cross-validation at two tropical forest sites in French Guiana. *Remote Sensing of Environment, 175*, 138-147

Nannini, M., & Scheiber, R. (2006). A time domain beamforming algorithm for SAR tomography. In *Proc. EUSAR* (pp. 1-4)

Nannini, M., & Scheiber, R., & Horn, R., & Moreira, A. (2011). First 3-D reconstructions of targets hidden beneath foliage by means of polarimetric SAR tomography. *IEEE Geoscience and Remote Sensing Letters*, *9*(1), 60-64

Nouvel, J. F., Herique, A., Kofman, W., & Safaeinili, A. (2005). Radar signal simulation: Surface modeling with the Facet Method. *Radio Science, 39*(1), 1-17

Nozette, S. *et al.* (2010). The Lunar Reconnaissance Orbiter Miniature Radio Frequency (Mini-RF) technology demonstration, *Space Science Review*, 150, 286–302

Picardi, G. *et al.* (2005). Radar soundings of the subsurface of Mars. *Science*, *310*(5756), 1925-1928

Reigber, A. & Moreira, A. (2000). First demonstration of airborne SAR tomography using multibaseline L-band data. *IEEE Transactions on Geoscience and Remote Sensing*, *38*(5), 2142-2152.

Seu, R. *et al.* (2007). SHARAD sounding radar on the Mars Reconnaissance Orbiter. *Journal of Geophysical Research: Planets*, *112*(E5)

Soumekh, M. (1999). Synthetic aperture radar signal processing (Vol. 7). *New York: Wiley.*

Ulaby, F. T., Moore, R., & Fung, A. K. (1986). Microwave remote sensing: Active and passive. Volume 3-From theory to applications

Ulander, L. M. & Frolind, P. O. (1998). Ultra-wideband SAR interferometry. , *IEEE transactions on geoscience and remote sensing*, *36*(5), 1540-1550.

Van den Berg, E. & Friedlander, M. P. (2011). Sparse optimization with least-squares constraints. *SIAM Journal on Optimization*, *21*(4), 1201-1229

Van den Berg, E. & Friedlander, M. P. (2007). SPGL1: A solver for large-scale sparse reconstruction.

Walsh, K. J., & Richardson, D. C. (2008). A steady-state model of NEA binaries formed by tidal disruption of gravitational aggregates. *Icarus*, *193*(2), 553-566,

Zhu, X. X., & Bamler, R. (2010) Very high resolution spaceborne SAR tomography in urban environment. *IEEE Transactions on Geoscience and Remote Sensing*, *48*(12), 4296-4308